DEVELOPMENT AND APPLICATION OF SURFACE MICRO PARTICLES AS LOCAL TEMPERATURE SENSORS

by

Brian Squires, B.S.

A thesis submitted to the Graduate Council of
Texas State University in partial fulfillment
of the requirements for the degree of
Master of Science
with a Major in Physics
August 2016

Committee Members:

Mark Holtz (chair)

Todd Hudnall

Casey Smith

FAIR USE AND AUTHOR'S PERMISSION STATEMENT

Fair Use

Duplication Permission

ACKNOWLEDGEMENTS

I would like to thank my committee members Dr. Mark Holtz, Dr. Todd Hudnall, and Dr. Casey Smith for their support and for pushing me to be a better scientist. I would like to acknowledge my colleagues Dr. Mohammad Nazari, Dr. Sandeep Sohal, and Logan Hancock for their help and support. I would like to thank Texas State University, NRL, and DARPA for financial support.

TABLE OF CONTENTS

Page

LIST OF FIGURES

Figure **Page**

LIST OF ABBREVIATIONS

Abbreviation	Description
CVD	chemical vapor deposition
h-BN	hexagonal boron nitride
HEMT	high electron mobility transistor
TDTR	time-domain thermal reflectance

I. INTRODUCTION

With rapidly increasing power densities in high electron mobility electronic devices, device self-heating is a growing concern. Proper thermal management is imperative to maintain device efficiency and mitigate device failure. A proposed solution is to place devices in intimate thermal contact with a good thermal conductor, such as diamond. Modern chemical vapor deposition (CVD) diamond growth has greatly improved the quality of synthetic diamond thin films, but the first few hundred nanometers (called the nucleation layer) is still very poor.[1] Particularly, due to the morphology of the diamond polycrystals, the lateral thermal conductivity of CVD is very low compared to single crystals.[1,2] In order to optimize the thermal management of devices using diamond, it is imperative to understand the thermal properties of CVD diamond thin films.

Thermal conductivity values for diamond thin films have been measured previously.[1,2] However, the devices used in this measurement are subject to an anisotropic stress gradient due to the thermal expansion mismatch between diamond and the metal heater and substrate. In this work, the lateral thermal conductivity of a CVD diamond thin film is interrogated via micro-Raman mapping of temperature distribution near a fabricated micro-heater. Additionally, in order to eliminate stress as a source of error, hexagonal boron nitride (h-BN) nano/micro-particles are deposited on the diamond surface to be used as stress-free Raman temperature probes.

A novel technique for depositing h-BN nano/micro-particles is developed in this work. A suspension of h-BN in ethylene glycol is dropped into a bead of methanol

that is placed on the sample. The difference in surface tension between methanol and ethylene glycol triggers precipitation of h-BN particles onto the sample surface. This technique is mild enough to be used on sensitive samples. Additionally, the temperature probes may be deposited on any surface in order to map surface temperature. This may prove to be an invaluable tool for temperature measurement of fully metalized, or even packaged electronic devices

II. BACKGROUND

The accurate determination of local temperatures of devices is important for understanding how to efficiently mitigate device self-heating. Device self-heating plagues all electronic devices, including silicon MOSFET's,[3] laser diodes,[4,5] and high electron mobility transistors (HEMT's).[6–10]

One technique for measuring temperature involves placing a thermocouple in physical contact with the system to be studied. Resistive micro-heaters may be fabricated on the surface of a device.[10,11] These contact thermometers are limited in the sense that they can only measure the temperature at a fixed location. Non-contact optical methods are nondestructive and have the freedom to measure multiple local temperatures on a single device. Many measurements of thermal conductivity rely on transient measurements such as time domain thermal reflectance (TDTR).[2,8] This technique requires the sample to be coated with an aluminum transducer layer that may impede the functionality of the device. Infra-red microscopy can be used to map temperatures in an operating device.[12] However, the spatial resolution of this method is poor. Additionally, thermal conductivity can be measured by holographic interferometry.[13] The luminescence intensity and lifetime of materials can be exploited to determine temperature. Fluorescent nanoparticles are often used to determine local temperatures of physiological samples.[14]

Many Raman spectroscopy techniques have been developed to determine local temperature rises in materials. One such optical method involves measuring the intensity ratio of the Stokes and anti-Stokes peaks.[15] This measurement,

however, is perturbed by electric field induced non-equilibrium longitudinal-optical phonons and is therefore unfit for measuring temperatures of driven devices.[15] Additionally, this technique requires a very broad spectral range that straddles the laser line. The Raman linewidth of specific materials is sensitive to temperature and can be used to characterize temperatures in crystalline materials.[16] This sensitivity is weak, however, making accurate temperature measurements using Raman linewidth somewhat challenging. Additionally, local stresses greatly perturb the Raman linewidth, invalidating this technique for measurement of polycrystalline samples, such as CVD diamond thin films.

Kuball et. al. have demonstrated that materials deposited on a surface may act as micro-Raman surface temperature probes.[1,17] Micro-diamonds deposited on the surface of a device serve to accurately and rapidly measure the surface temperature of the device.[17] Specifically, a micro-diamond suspension in ethanol was deposited on HEMT device. Diamond particles present on the gate were used as Raman probes to measure the surface temperature. Moreover, the Raman setup was equipped with an acousto-optical modulator to perform time-resolved Raman thermography. Although this method has proven to work well, it is not possible to measure diamond surface temperatures. Another proven method is to use silicon nanowires as surface temperature probes.[1] However, the heat flow through the length of the wire may confound a measurement of lateral thermal conductivity. Additionally, proper care must be taken to ensure there is no local heating in the nanowire; the laser energy is above the silicon bandgap, therefore absorption will cause the silicon to heat. This is alleviated by reducing the laser power such that

there is no local heating. In this work, the use of a material with a much higher bandgap eliminates the concern for laser heating the micro/nano particle temperature sensors.

III. MATERIALS

3.1 Diamond

Diamond has a crystal structure that can be thought of as two interpenetrating face-centered cubic Bravais lattices offset by ¼ of the unit cell diagonal. Although the structure is loosely packed (the atomic packing factor is 34%), diamond has a remarkable hardness. Each atom is sp^3 hybridized, and sits at the corner of a tetrahedron, as shown in Figure 1. This configuration lends to extremely strong bonds. Additionally, due to the light atomic mass and strong bonds, diamond has an enormous Debye temperature (2230K)[18], the temperature at which all phonon modes are excited. Diamond is an insulator with an indirect bandgap at ~5.4 eV. The heat carriers in diamond are therefore exclusively phonons. Because carbon atoms are light, the phonon energies in diamond are very high, resulting in a high thermal conductivity of ~3320 W/m*K for isotopically enriched synthetic diamond.[19]

3.2 Diamond Synthesis

Diamond, both natural and synthetic, is produced under extremely high temperature and pressure. In the synthetic case, this process mimics the natural process, producing high quality stress free diamond. This is however not a useful technique in the semiconductor industry in which the substrate is often fragile.

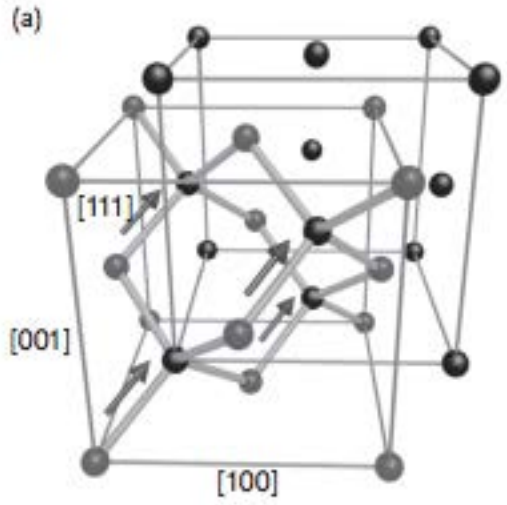

Figure 1: Diamond crystal structure. The cell is cubic with a lattice constant of 3.57 Å. Shown are the two interpenetrating FCC lattices. The arrows indicate the relative movement of the zone centered optical phonon involved in first order Raman scattering in diamond.[20]

Also, this method of diamond growth is very costly. To avoid such harsh environments, it is possible to grow diamond synthetically via chemical vapor deposition (CVD). In CVD diamond growth, a substrate is coated with a nano-diamond powder seed layer and placed in a high vacuum. A dilute mixture of methane and hydrogen are slowly introduced into the chamber via an inert carrier gas (nitrogen or argon). Some of the molecular hydrogen gas is converted to atomic hydrogen by application of microwave energy, an electric discharge, or a hot filament. The gasses react with the diamond seeds causing them to grow. Eventually, the seed crystals merge, causing the lateral growth to cease. As the diamond film grows thicker, the crystal domains join together and the grain boundaries become less distinct. However, the first few hundred nanometers of growth are riddled with defects, domain boundaries, and non-diamond carbon materials, significantly influencing the material properties in this region.

Diamond has a single zone-centered optical phonon centered around 1333 cm^{-1}. This phonon has a relatively large Raman cross-section that is, as usual, dependent on the incident radiation frequency.[20,21] The phonon frequency is dependent on temperature and stress, making it a useful tool for material characterization. The lifetime of this phonon, and thus the Raman linewidth, is also dependent on such parameters, but will not be discussed in this work. The Raman sensitivity of diamond (sp^3) increases as the incident wavelength approaches the UV, whereas non-diamond carbon (sp^2) is more sensitive to higher wavelengths (approaching infrared).[22]

3.3 Hexagonal Boron Nitride

Hexagonal boron nitride (h-BN) adopts a one-atom thick hexagonal crystal structure similar to graphene with lattice sites alternating between boron and nitrogen. Like diamond, it is an insulator with an indirect band gap of 5.955 eV.[23] Unlike diamond, it is readily available in particle form, making it attractive as a nano/micro sensor. It is very chemically and thermally robust.

h-BN has a zone-centered optical phonon that is centered around ~1366 cm^{-1}. There is an additional Raman active optical phonon centered around 55 cm^{-1}; it is very weak and will not be discussed in this work. The E_{2g} symmetric phonon centered around 1366 cm^{-1} has an empirically high Raman temperature coefficient (0.02025 ± 0.00030 $cm^{-1}/°C$), which makes it highly valuable for use as a surface temperature Raman probe.

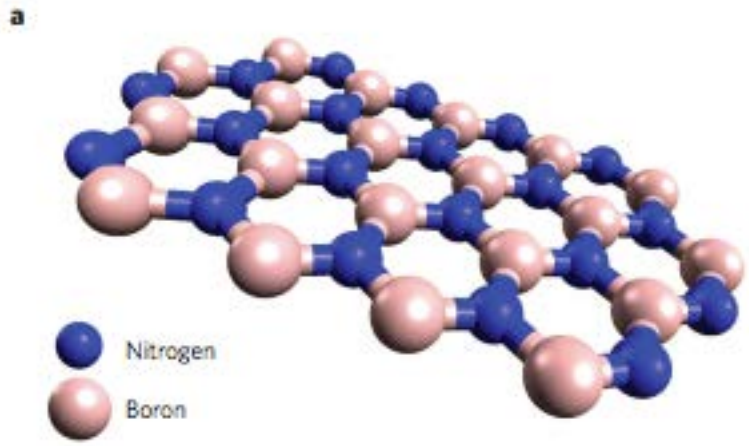

Figure 2: Hexagonal boron nitride crystal structure.[24]

IV. THEORY

Raman spectroscopy is a useful tool for characterizing materials due to its nondestructive nature. In Raman scattering, incident light is scattered inelastically, where the energy difference is due to the annihilation or creation of a phonon (Stokes and Anti-Stokes, respectively). The Raman shift, line width, polarization, and intensity can all provide valuable information about the material including chemical identification, stress and strain, doping concentration, local temperature, and more.

The goal of this chapter is to elucidate the lattice dynamics that gives rise to phonon dispersion relations. Next, classical and quantum derivations of Raman scattering will be introduced. Additionally, the applications of Raman spectroscopy will be discussed.

4.1 Harmonic Approximation of Lattice Dynamics

Phonons are the collective normal mode vibrations in condensed phases of matter. Due to their quantized nature, phonons are described as quasiparticles. The following derivation of lattice dynamics and Raman theory relies heavily on Sampriti Bagchi's work on Raman characterization of anharmonicity and alloying effects in semiconductors.[25] In nonmetallic materials, vibrational energies are well separated from electronic energy levels. Therefore, we can employ the Born-Oppenheimer approximation to describe the eigenfunctions of the coupled system as the product of vibrational and electronic wavefunctions:

$$\boldsymbol{\Psi_{nv}(x,u) = \psi_{nv}(u)\phi_n(x,u)} \quad (1)$$

where $\psi_{\boldsymbol{nv}}(\boldsymbol{u})$is the vibrational wave function, $\phi_{\boldsymbol{n}}(\boldsymbol{x},\boldsymbol{u})$is the many body electronic wavefunction, n and v are the principle electronic and vibrational quantum numbers, respectively, and $\boldsymbol{x}$ and $\boldsymbol{u}$are the electronic coordinates and nuclear displacement, respectively. The electronic wavefunctions is given by solving the many-electron Schrodinger equation:

$$[T_E + V_{EE}(\boldsymbol{x}) + V_{EN}(\boldsymbol{x},\boldsymbol{u}) + V_{NN}(\boldsymbol{u})]\,\phi_n(\boldsymbol{x},\boldsymbol{u}) = E_n(\boldsymbol{u})\phi_n(\boldsymbol{x},\boldsymbol{u}) \tag{2}$$

where T_E is the electronic kinetic energy, $V_{EE}(\boldsymbol{x})$ is the electron-electron interaction potential, $V_{EN}(\boldsymbol{x},\boldsymbol{u})$ is the electron-lattice potential, and $V_{NN}(\boldsymbol{u})$ is the nuclear-nuclear potential, and $E_n(\boldsymbol{u})$ is the n^{th} electronic eigenenergy. Employing the adiabatic approximation, wherein the system remains in the many-electron ground state as the lattice moves, the effective potential (crystal potential) is taken to be equal to the electronic ground state energy eigenvalue:

$$V(\boldsymbol{u}) = E_0(\boldsymbol{u}) \tag{3}$$

The equilibrium configuration of the lattice is given by the minimum of the crystal potential. The displacements of the atoms are given as a 3n x N dimensional vector

$$\boldsymbol{u} \equiv \{u_\alpha(l,k)\} \tag{4}$$

where l =1,…N indexes the unit cells of the crystal, k indexes each atom in the unit cell, and α indexes the spatial position of the atom in the cell (x,y,z).

It is useful to expand the crystal potential as a Taylor series in small displacements from equilibrium.

$$V(\boldsymbol{u}) = V_0 + \sum_{\alpha,l,k} \frac{\partial V}{\partial u_\alpha(l,k)}\Big|_0 u_\alpha(l,k) +$$

$$\sum_{\alpha,l,k}\sum_{\beta,l',k'} \frac{\partial^2 V}{\partial u_\alpha(l,k)\partial u_\alpha(l,k)}\Big|_0 u_\alpha(l,k)u_\beta(l',k') + \cdots \quad (5)$$

V_0 is a constant representing the binding energy of the crystal, and thus can be set to zero when discussing the dynamics of lattice vibration. The second term is equal to zero because the forces at equilibrium are zero. Therefore, the first non-vanishing term is the quadratic term, giving rise to what is known as the harmonic approximation. Higher order terms in the expansion give rise to anharmonic behavior such as thermal expansion and pressure dependent elastic constants.[18,26] The potential energy in the harmonic approximation is therefore given by

$$V = \frac{1}{2}\sum_{\alpha,l,k}\sum_{\beta,l',k'} \boldsymbol{\Phi}\, u_\alpha(l,k)u_\beta(l',k') \quad (6)$$

where $\boldsymbol{\Phi}$ is a 3nN x 3nN interatomic force matrix given by the second derivatives with respect to displacement evaluated at equilibrium

$$\boldsymbol{\Phi} \equiv \left\{\frac{\partial^2 V}{\partial u_\alpha(l,k)\partial u_\alpha(l,k)}\Big|_0\right\} \quad (7)$$

The vibrational Hamiltonian can then be written as

$$H = \frac{1}{2}(\boldsymbol{p}^\dagger \boldsymbol{M}^{-1}\boldsymbol{p} + \boldsymbol{u}^\dagger \boldsymbol{\Phi}\boldsymbol{u}) \quad (8)$$

Where **M** is the diagonal matrix of masses

$$\boldsymbol{M} = m_k \delta_{ll'} \delta_{kk'} \delta_{\alpha\beta} \tag{9}$$

The equations of motion of the atoms are given by setting the force on the k^{th} atom equal to the negative derivative of the crystal potential.

$$m_k \ddot{u}_\alpha(l,k) = -\frac{\partial V}{\partial u_\alpha(l,k)} = V = \frac{1}{2}\sum_{\beta,l',k'} \boldsymbol{\Phi}\, u_\beta(l',k') \tag{10}$$

Note that previously this first derivative was evaluated at equilibrium in order to arrive at the harmonic approximation. Currently, however, this derivative is *not* evaluated at equilibrium, as that would yield the trivial solution in which there is no lattice vibration. This equation is a second order homogeneous ordinary differential equation, thus it is valid to assume an oscillatory solution of the form

$$u_{lk}(\boldsymbol{q},\omega) = u_{lk} e^{i[\boldsymbol{q}\cdot\boldsymbol{R}(l)-\omega t]} \tag{11}$$

The normal mode frequencies are then the solution to the eigenvalue equation

$$\left(\boldsymbol{\Phi} - \omega_f \boldsymbol{M}\right)\boldsymbol{\psi}(f) = 0 \tag{12}$$

where f=1…3Nn indexes the normal modes, and $\boldsymbol{\psi}(f) = \psi(l\alpha|f)$ is the eigenvector of the corresponding lattice vibration with frequency ω_f.

Because the matrices $\boldsymbol{M}$ and $\boldsymbol{\Phi}$ are Hermitian, they must satisfy the following conditions of orthonormality and completeness:

$$\boldsymbol{\psi}^\dagger(f)\boldsymbol{M}\boldsymbol{\psi}(f') = \delta_{ff'} \tag{13}$$

and

$$\sum_{f=1}^{3nN} \boldsymbol{M}\boldsymbol{\psi}(f)\boldsymbol{\psi}(f') = \boldsymbol{I} \tag{14}$$

where $\boldsymbol{I}$ is the identity matrix. With these conditions, it is appropriate to write $\boldsymbol{u}$ as a linear combination of the eigenvectors $\boldsymbol{\psi}$ such as

$$\sum_f \boldsymbol{\psi}(f) Q_f \tag{15}$$

where Q_f are the normal coordinates of the crystal, defined as

$$Q_f = \boldsymbol{\psi}^{\dagger} \boldsymbol{M} \boldsymbol{u}^* \tag{16}$$

The Hamiltonian can now be rewritten in terms of the dimensionless normal coordinates Q_f.

$$H = \frac{1}{2}\sum_f \left(\dot{Q}_f^2 + \omega_f^2 Q_f^2\right) \tag{17}$$

The equation of motion then becomes

$$\ddot{Q}_f + \omega_f Q_f = 0 \tag{18}$$

To describe the dynamics using quantum mechanics, the operators Q_f and $\dot{Q}_f$ must satisfy the commutation relation $\left[Q_f, \dot{Q}_{f'}\right] = i\hbar\delta_{ff'}$. In the language of second quantization, the vibrational Hamiltonian can be written as

$$H = \sum_f \hbar\omega_f \left(a_f^{\dagger} a_f + \frac{1}{2}\right) \tag{19}$$

where $a_f^{\dagger}$ and a_f are the creation and annihilation ladder operators

$$a_f = \frac{1}{\sqrt{2\hbar\omega_f}}\left(\dot{Q}_f - i\omega_f Q_f\right) \tag{20}$$

The mode frequencies and eigenvectors are solutions to the eigenvalue equation (12) which can be rewritten as

$$\sum_{l',k',\beta}\left[\phi_{\alpha\beta}(lk,l'k') - \omega_f^2 m_k \delta_{ll'}\delta_{kk'}\delta_{\alpha\beta}\right]\psi(l'k'\beta|f) = 0 \tag{21}$$

Using Bloch's theorem, the solution can be written as plane waves

$$\psi_\alpha(lk|\boldsymbol{q}j) = \frac{e_\alpha(k|\boldsymbol{q}j)}{\sqrt{NM(k)}} e^{i\boldsymbol{q}\cdot\boldsymbol{R}(lk)} \tag{22}$$

where $\mathbf{R}(lk)$ indicates the equilibrium lattice vector corresponding to the k[th] atom in the l[th] primitive cell. The phonon polarization vectors

$$\{e_\alpha(k|\boldsymbol{q}j)\} \equiv \boldsymbol{e}(\boldsymbol{q}j) \tag{23}$$

satisfy the orthonormality condition

$$\boldsymbol{e}^\dagger(\boldsymbol{q}j)\boldsymbol{e}(\boldsymbol{q}j') = \delta_{jj'} \tag{24}$$

where j=1,2,3,…3n index the phonon polarization branches.

Equation (21) can now be written as

$$\sum_{l'k'\beta}\frac{\phi_{\alpha\beta}(lk,l'k')}{\sqrt{m_k m_{k'}}} e^{\left[i\boldsymbol{q}\cdot\boldsymbol{R}(\boldsymbol{l'k'})\right]} e_\beta(k'|\boldsymbol{q}j) = \omega_f^2 e^{i\boldsymbol{q}\cdot\boldsymbol{R}(lk)} e_\alpha(k|\boldsymbol{q}j) \tag{25}$$

More compactly, the previous equation can be written as

$$\sum_{kk'}\left[D_{\alpha\beta}(kk'|\boldsymbol{q}) - \omega^2(\boldsymbol{q})\delta_{kk'}\delta_{\alpha\beta}\right]e(kk'|\boldsymbol{q}j) = 0 \tag{26}$$

where

$$D_{\alpha\beta}(kk'|\boldsymbol{q}) = \frac{1}{\sqrt{m_k m_{k'}}} \sum_{l'} \phi_{\alpha\beta}(lk, l'k') e^{[i\boldsymbol{q}\cdot(\boldsymbol{R}(l)-\boldsymbol{R}(l'))]} \tag{27}$$

This can be written in matrix form as

$$[\boldsymbol{D}(\boldsymbol{q}) - \omega^2(\boldsymbol{q})\boldsymbol{I}]\boldsymbol{e}(\boldsymbol{q}j) = 0 \tag{28}$$

where ***D(q)*** is known as the dynamical matrix. For non-trivial solutions, the following determinant must vanish:

$$\det[\boldsymbol{D}(\boldsymbol{q}) - \omega^2(\boldsymbol{q})\boldsymbol{I}] = 0 \tag{29}$$

The solutions to this equation yield the phonon dispersion relations in *k*-space, as shown in Figure 2.

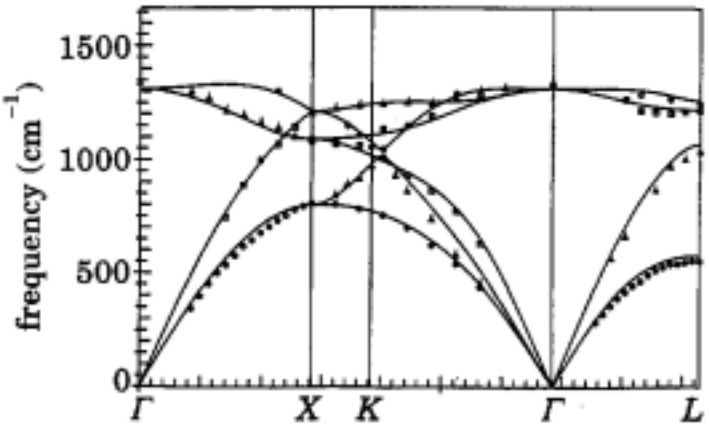

Figure 3: Phonon dispersion of diamond. The solid lines indicate *ab-initio* calculated spectra, whereas the points are neutron scattering data. [27]

4.2 Raman Scattering

Incoherent light scattering (Rayleigh and Raman) is considered to be due to oscillating electric and magnetic multipole moments of the material induced by the incident electromagnetic waves. This statement holds for both the classical and quantum treatment of Raman scattering described in the following sections.

4.2.1 Classical Treatment

The following treatment is modeled after Derek Long's work, *The Raman Effect*.[28] In classical electrodynamics it is well known that an oscillating electric (or magnetic) multipole will emit electromagnetic radiation. As such, it is important to understand the dynamics of the induced dipole moment of the material due to incident radiation. The total time-dependent electric dipole moment can be expanded in terms of electric field perturbations as

$$\boldsymbol{p} = \boldsymbol{p}^{(1)} + \boldsymbol{p}^{(2)} + \boldsymbol{p}^{(3)} + \cdots \tag{30}$$

where $\boldsymbol{p}^{(1)} \gg \boldsymbol{p}^{(2)} \gg \boldsymbol{p}^{(3)}$, so the series converges rapidly. These perturbative terms are expressed as functions of the electric field as

$$\boldsymbol{p}^{(1)} = \boldsymbol{\alpha} \cdot \boldsymbol{E} \tag{31}$$

$$\boldsymbol{p}^{(2)} = \frac{1}{2}\boldsymbol{\beta} : \boldsymbol{EE} \tag{32}$$

$$\boldsymbol{p}^{(3)} = \frac{1}{6}\boldsymbol{\gamma} \vdots \boldsymbol{EEE} \tag{33}$$

where $\boldsymbol{\alpha}$ is the second rank polarizability tensor, $\boldsymbol{\beta}$ is the third rank hyperpolarizability tensor, and $\boldsymbol{\gamma}$ is the fourth rank second-hyperpolarizability

tensor. Note that in the above equations, the electric field is written in matrix form. The hyperpolarizability and second-hyperpolarizability terms describe two and three photon processes and will be neglected in this treatment.

Light incident on a material will induce an oscillating dipole moment. If additional vibrations (phonons) are created or annihilated in this process, the scattered light will contain a sum or difference of the combined oscillatory processes. Classically, this can be described by expanding the components of the polarizability tensor in terms of small perturbations of the normal coordinates as

$$\alpha_{\rho\sigma} = \left(\alpha_{\rho\sigma}\right)_0 + \sum_k \left(\frac{\partial \alpha_{\rho\sigma}}{\partial Q_k}\right)_0 Q_k + \sum_{k,l} \left(\frac{\partial^2 \alpha_{\rho\sigma}}{\partial Q_k \partial Q_l}\right)_0 Q_k Q_l + \cdots \tag{34}$$

Assuming harmonic motion, the normal coordinates Q_k have a time dependence

$$Q_k = Q_{k_0} \cos(\omega_k t + \delta_k) \tag{35}$$

where ω_k is the frequency of the k^{th} vibrational mode and δ_k is a phase factor. Here, we introduce a derived polarizability tensor $\boldsymbol{\alpha'_k}$ which has components

$$\left(\alpha'_{\rho\sigma}\right)_k = \left(\frac{\partial \alpha_{\rho\sigma}}{\partial Q_k}\right)_0 \tag{36}$$

in order to rewrite the polarizability tensor with explicit time dependence as

$$\boldsymbol{\alpha_k} = \boldsymbol{\alpha_0} + \boldsymbol{\alpha'_k} Q_{k_0} \cos(\omega_k t + \delta_k) \tag{37}$$

The incident electric field also has a time dependence:

$$\boldsymbol{E} = \boldsymbol{E_0} \cos(\omega_\gamma t) \tag{38}$$

where $\omega_\gamma$is the frequency of the incident light. Inserting this into the first order dipole vector equation,

$$\boldsymbol{p}^{(1)} = [\boldsymbol{E_0}\cos(\omega_\gamma t)] * [(\boldsymbol{\alpha_0} + \boldsymbol{\alpha'_k} Q_{k_0}\cos(\omega_k t + \delta_k)] =$$

$$\boldsymbol{\alpha_0 E_0}\cos(\omega_\gamma t) + \boldsymbol{\alpha'_k E_0} Q_{k_0}\cos(\omega_k t + \delta_k)\cos(\omega_\gamma t) \tag{39}$$

The second term can be simplified using the trigonometric identity

$$\cos(A)\cos(B) = 1/2\,[\cos(A+B) + \cos(A-B)] \tag{40}$$

so that

$$\boldsymbol{p}^{(1)} = \boldsymbol{\alpha_0 E_0}\cos(\omega_\gamma t) + \tfrac{1}{2}\boldsymbol{\alpha'_k E_0} Q_{k_0}\cos(\omega_\gamma + \omega_k + \delta_k)$$

$$+\tfrac{1}{2}\boldsymbol{\alpha'_k E_0} Q_{k_0}\cos(\omega_\gamma - \omega_k - \delta_k) \tag{41}$$

The first term in this expression describes Rayleigh scattering, whereas the second and third terms describe Stokes and Anti-Stokes Raman scattering, respectively. It should be noted that the induced dipole for Rayleigh scattering is in phase with the incident field, whereas the dipole involved with Raman scattering is phase shifted by δ_k, which is the phase of the material dependent normal mode Q_k. This has important implications regarding the relative intensities of Rayleigh and Raman radiation. The incident radiation, oscillating at ω_γ , induces an electric dipole in the material which also oscillates at ω_γ, giving rise to Rayleigh scattering. In Raman scattering, however, this oscillating dipole is modulated by a lattice vibration of a

different phase such that the radiated wave is analogous to a beat frequency between the two.

4.2.2 Quantum Treatment

Although the classical model for Raman scattering is fairly simple and intuitive, it lacks the breadth of a complete theory. The following section introduces a quantum mechanical theory of inelastic scattering of light by crystals.

The total Hamiltonian for a process in which light is scattered from a medium can be written as the sum of three terms

$$\hat{H} = \hat{H}_e + \hat{H}_\gamma + \hat{H}_L + \hat{H}_{e\gamma} + \hat{H}_{eL} \tag{42}$$

where $\hat{H}_e$ is the electron Hamiltonian, $\hat{H}_\gamma$ is the photon Hamiltonian, $\hat{H}_L$ is the lattice vibration Hamiltonian, $\hat{H}_{e\gamma}$ is the electron-photon interaction Hamiltonian, and $\hat{H}_{eL}$ is the electron-phonon interaction Hamiltonian. $\hat{H}_e + \hat{H}_\gamma + \hat{H}_L$ is considered here to be the zeroth-order approximation.[29] The electron-photon interaction Hamiltonian can be written as

$$\hat{H}_{e\gamma} = \frac{e^2}{2m}\sum_j \hat{\boldsymbol{A}}(\boldsymbol{r}_j)\cdot\hat{\boldsymbol{A}}(\boldsymbol{r}_j) + \frac{e}{m}\sum_j \hat{\boldsymbol{A}}(\boldsymbol{r}_j)\cdot\hat{\boldsymbol{p}}_j \tag{43}$$

where $\hat{\boldsymbol{A}}(\boldsymbol{r}_j)$ is the second-quantized radiation vector potential and $\hat{\boldsymbol{p}}_j$ is the momentum operator of the j^{th} electron. Note that because the vector potential operator is written in the second-quantization approach, the photon creation and annihilation operators are embedded within it. The first term in this Hamiltonian

relates to scattering by electronic transitions in which the initial and final state is in the same band.[30]

The matrix element corresponding to a first order Raman scattering process is given by

$$K_{fi} = \sum_{\alpha,\beta} \frac{\langle f|\hat{H}_{e\gamma}|\beta\rangle\langle\beta|\hat{H}_{eL}|\alpha\rangle\langle\alpha|\hat{H}_{e\gamma}|i\rangle}{(E_\beta - \hbar\omega_f)(E_\alpha - \hbar\omega_i)} + \cdots \quad (44)$$

where the omitted terms all of the time ordering permutations. Note that the time ordering goes from right to left. In this first term, a photon is absorbed by the material and promotes an electron to an intermediate state α. Next, the electron interacts with the lattice, either creating or annihilating a phonon, resulting in *different* intermediate state β. (The adiabatic approximation can be employed here to assume $|\alpha\rangle = |\beta\rangle$.) This state then transitions to the final state, emitting the scattered photon. The permuted time ordering terms (not shown) have a low transition probability, but must be accounted for when deriving transition rates and scattering cross-sections. In this form, it is easy to see that the transition probability has a direct dependence on the incident radiation frequency; as the incident energy approaches the band gap energy, the transition probability approaches a large value. This gives rationality for using UV (363.8 nm) as opposed to visible (514.5 nm) excitation for Raman studies of high bandgap semiconductors such as diamond and hexagonal boron nitride.

The transition probability per unit time can be calculated via Fermi's golden rule as

$$W_{fi} = \frac{2\pi}{\hbar}\left|K_{fi}\right|^2 \delta\left(E_i - E_f\right) \tag{45}$$

We can define the microscopic scattering cross-section as the transition probability per unit time divided by the photon velocity in the medium[29]

$$d\sigma = \frac{\sum_{f,i} W_{fi}}{v_g} \tag{46}$$

Substitution into Fermi's golden rule yields

$$d\sigma = \frac{2\pi}{\hbar v_g}\sum_{\boldsymbol{k}_f}\sum_{E_i,E_f}\left|K_{f,i}\right|^2 \delta\left(\hbar\omega_f + E_f - \hbar\omega_i - E_i\right) \tag{47}$$

where the first summation is restricted to a shell in k-space defined by the solid angle $d\Omega$ and between ω_f and $\omega_f + d\omega_f$. Thus, we can make the substitution

$$\sum_{\boldsymbol{k}_f} 1 = \frac{k_f^2 dk_f d\Omega}{(2\pi)^3} = \frac{n^3\left(\hbar\omega_f\right)^2 d\left(\hbar\omega_f\right) d\Omega}{(2\pi)^3 c^3 \hbar^3} \tag{48}$$

where the last equality derives from the substitution $k = \frac{n\omega}{c}$. Inserting this into the equation for the scattering cross-section yields

$$d\sigma = \frac{n^3\left(\hbar\omega_f\right)^2 d\left(\hbar\omega_f\right) d\Omega}{4\pi^2 c^3 \hbar^4 v_g}\sum_{E_f,E_i}\left|K_{f,i}\right|^2\left(\hbar\omega_i + E_i - E_f\right)^2 \tag{49}$$

Now, the sum over E_f and E_i is restricted to $\hbar\omega_f < \hbar\omega_i + E_i - E_f < \hbar\left(\omega_f + d\omega_f\right)$ due to the Dirac delta function.

4.2.3 Kinematics of Raman Scattering

Although Raman scattering is inelastic, energy and momentum conservation still hold when discussing crystalline materials. Conservation of energy requires that

$$\omega = \omega_I - \omega_S \tag{50}$$

where ω is the scattered frequency, ω_I is the incident radiation frequency, and ω_S is the Stokes component frequency. A similar equality holds for the anti-Stokes component. This process must also conserve momentum, such that

$$\hbar \boldsymbol{q} = \hbar \boldsymbol{k_I} - \hbar \boldsymbol{k_S} \tag{51}$$

where $\hbar \boldsymbol{q}$ represents the phonon momentum, and $\boldsymbol{k_I}$ and $\boldsymbol{k_S}$ are the incident and scattered photon momenta in the medium, respectively.

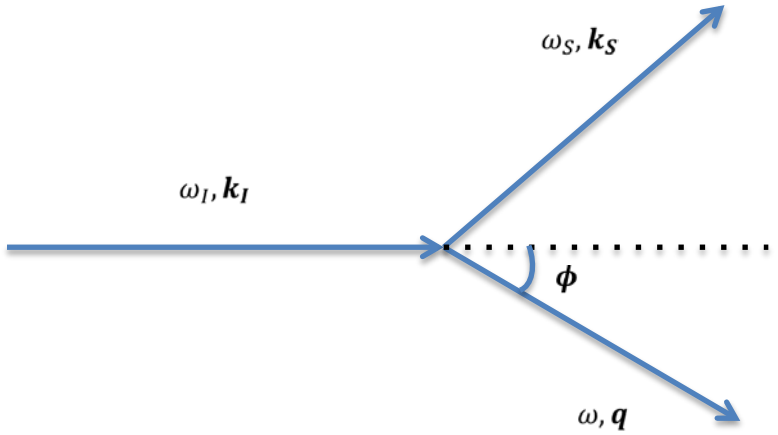

Figure 4: Momentum conservation in stokes scattering.

Light used in typical scattering experiments has a frequency of approximately $\frac{\omega_I}{2\pi} \approx 5 * 10^{14}$ Hz.[30] Assuming an approximate refractive index of 1.5, the wavevector corresponding to the incident radiation is $k_I \approx 1.5 * 10^7\ \mathrm{m}^{-1}$. The range of wavevectors accessible to light scattering experiments is approximately

$$0 < q < 3 * 10^7\ \mathrm{m}^{-1}. \tag{52}$$

For a typical solid, the maximum wavevector in the first Brillouin zone (π/d) is typically of the order $3*10^{10}$ m^{-1}, three orders of magnitude above the upper limit of the radiation wavevectors. Therefore, $\omega \ll \omega_I$, an thus Raman scattering only probes phonons that are in the neighborhood $\boldsymbol{q} \approx 0$.

4.3 Anharmonic contributions to lattice dynamics

The harmonic approximation, although useful for determining phonon spectra, fails to predict temperature dependent phenomena such as thermal expansion, and the temperature and pressure dependence of phonons. We can describe the full crystal potential as the sum

$$V = V^{eq} + V^{harm} + V^{anh} \tag{53}$$

where the anharmonic term contains all of the higher order derivatives that were ignored in the harmonic approximation. The thermal conductivity of a material is dependent on the finite lifetime of the heat carriers (phonons) due to scattering. Phonon scattering is fundamentally described by the anharmonic term, V^{anh}, in equation (53). Classically, thermal conductivity is given by

$$\kappa = \frac{1}{3N_A} c_v n \langle v \rangle \lambda \tag{54}$$

where N_A is Avagadro's number, c_v is the constant volume heat capacity, n is the phonon occupation number, $\langle v \rangle$ is the thermal average phonon velocity, and λ is the phonon mean free path. The low temperature behavior ($T << T_D$), phonons scatter from defects and boundaries. At high temperature, phonon-phonon scattering plays

a large role in the thermal conductivity. The Debye temperature is high enough that, for this experiment, the phonon population does not reach a level at which phonon-phonon scattering is important. Therefore, the thermal conductivity studied here is mainly dependent on the impurity and boundary density of the sample.

Phonon frequencies are dependent on temperature as

$$\frac{d\omega}{dT} = \frac{\partial\omega}{dT} - \frac{\alpha}{\beta}\frac{\partial\omega}{dP} \tag{55}$$

where $\alpha = \frac{1}{V}\frac{\partial V}{\partial T}$ is the linear thermal expansion coefficient and $\beta = -\frac{1}{V}\frac{\partial V}{\partial P}$ is the compressibility.[31] The first term on the right is known as the explicit term and is fundamentally due to the phonon-phonon interaction. The second term is known as the implicit term, which arises from volume dilation due to changes in temperature. It is clear in this form that stress plays a crucial role in the temperature dependence of phonons. When the phonon frequency of the diamond thin film is measured as a function of temperature, it is the *total derivative* that is measured. Therefore, any stress that is produced by a measurement will impact the observed quantities. For instance, the thermal expansion mismatch between the gold/titanium heater and diamond will produce a compressive stress of roughly 0.22 GPa, based on COMSOL simulations. Because the bulk modulus, phonon pressure dependence, and other structural parameters are unknown in these samples, it is impossible to subtract the implicit term from the total derivative. In order to accurately measure the thermal conductivity of diamond thin films, it is necessary to determine temperature through a measurement that correctly accounts for the stress induced in diamond.

Nanoparticles deposited on the surface of the sample act as surface temperature probes that do not depend on the stress in the film.

4.4 Thermal Conductivity

Classically, heat flows in accordance with

$$\frac{dQ}{dt} = -\kappa \boldsymbol{A} \cdot \boldsymbol{\nabla} T \tag{56}$$

where $\frac{dQ}{dt}$ represents the heat flux, A is the cross sectional area vector, $\boldsymbol{\nabla} T$ is the temperature gradient, and κ is the thermal conductivity. When the quantity $\frac{dQ}{dt}$ is expressed in Watts, the units of κ are $W m^{-2} K^{-1}$. This experiment is conducted such that the heat flux is quasi-one-dimensional, so $\boldsymbol{\nabla} T$ can be reduced to $\frac{dT}{dx}$. The rate $\frac{dQ}{dt}$ can be reinterpreted as the dissipated power of the heater ($P = IV$). With these assumptions, we can rewrite

$$\kappa = C \frac{P}{A\left(\frac{dT}{dx}\right)} \tag{57}$$

where C is a correction factor to account for the geometry of the device. For devices for which heat flux will be symmetrically distributed, this factor should be $\frac{1}{2}$. For asymmetric devices, this factor is used to force the calculated thermal conductivity to be equivalent on either side of the heater, and is therefore given by

$$C = \frac{\left(\frac{dT}{dx}\right)_1}{\left(\frac{dT}{dx}\right)_1 + \left(\frac{dT}{dx}\right)_2} \tag{58}$$

V. EXPERIMENTAL

A Coherent argon ion laser was used with a wavelength of 363.8 nm. The beam was directed through a customized Olympus microscope with a 100x Mitutoya Plan Apo infinity corrected objective (N.A.=0.5). The beam was focused onto the sample to a ~3μm diameter spot. At maximum power, this gives a measured power at the sample of 1.1 mW and a . The emission was directed into a SPEX 1406 spectrometer with a single 1800 gr/mm diffraction grating. The signal was collected by a liquid nitrogen cooled Princeton Instruments CCD detector.

The samples used in this experiment, provided by the Naval Research Laboratory (NRL), were CVD diamond (nominally 1 micron thick) grown on a silicon substrate (~500 μm). The actual thickness of diamond was measured to be approximately 865 ± 15nm via spectroscopic and backscattering ellipsometry. Once the diamond was grown, channels were etched in the silicon from the back such that freestanding diamond membranes were formed. The diamond side of the wafer was then patterned with an approximately 100 nm titanium/gold stack to form micro-heaters, as shown in Figure 4. The width and length of each membrane is 200 and 1000 microns, respectively.

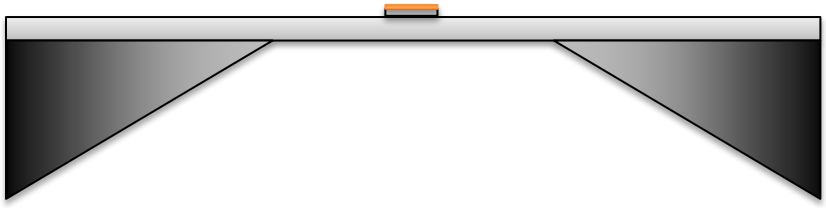

Figure 5: Side view of a typical diamond membrane on an NRL sample. The black region indicates the silicon substrate, the white indicates CVD diamond (approximately 1 micron thick), and the silver/gold indicates the Ti/Au heater stack (approximately 100 nm thick).

A meta-stable suspension was generated by charging a vial with ~50 mg of h-BN and 2-5 mL of ethylene glycol. The mixture was then placed in an ultrasonic bath for approximately five minutes to fully disperse h-BN platelets in the ethylene glycol. A bead (~0.5 mL) of methanol was carefully placed on the sample surface. A drop (~100 µL) of the h-BN-ethylene glycol suspension was dropped onto the methanol bead as shown in Figure 5. The difference in surface tension between the two solvents causes the suspension to collapse, precipitating small (approximately 200-1000 nm) particles of h-BN. This process was repeated until the desired number of particles was reached.

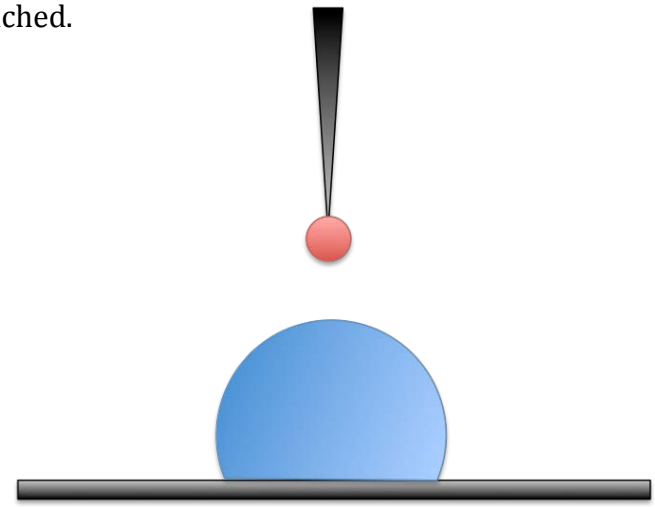

Figure 6: h-BN deposition method. A bead of methanol (blue) is deposited on the sample. A suspension of h-BN in ethylene glycol is dropped into the methanol bead via a micropipetter. The difference in surface tension between ethylene glycol and methanol collapses the suspension, precipitating h-BN micro-particles. The sample is then washed with methanol.

The Raman temperature coefficient (total derivative) was determined via a calibration method. The sample was placed on a Peltier thermoelectric heater stage in which a thermistor was embedded. The Raman shift for diamond was recorded for various substrate temperatures (measured by the calibrated thermistor) after allowing the stage to reach thermal equilibrium for approximately five minutes. The temperature was swept from room temperature to approximately 200 °C. The data was fit linearly to yield a Raman temperature coefficient of -0.01216 $\pm$ 0.00034 cm^{-1}/°C for the sample reported in this work, as shown in Figure 6. This was repeated for an h-BN microparticle located on the membrane, for which the temperature coefficient is 0.02025 $\pm$0.00030 cm^{-1}. These results are presented in Figure 7

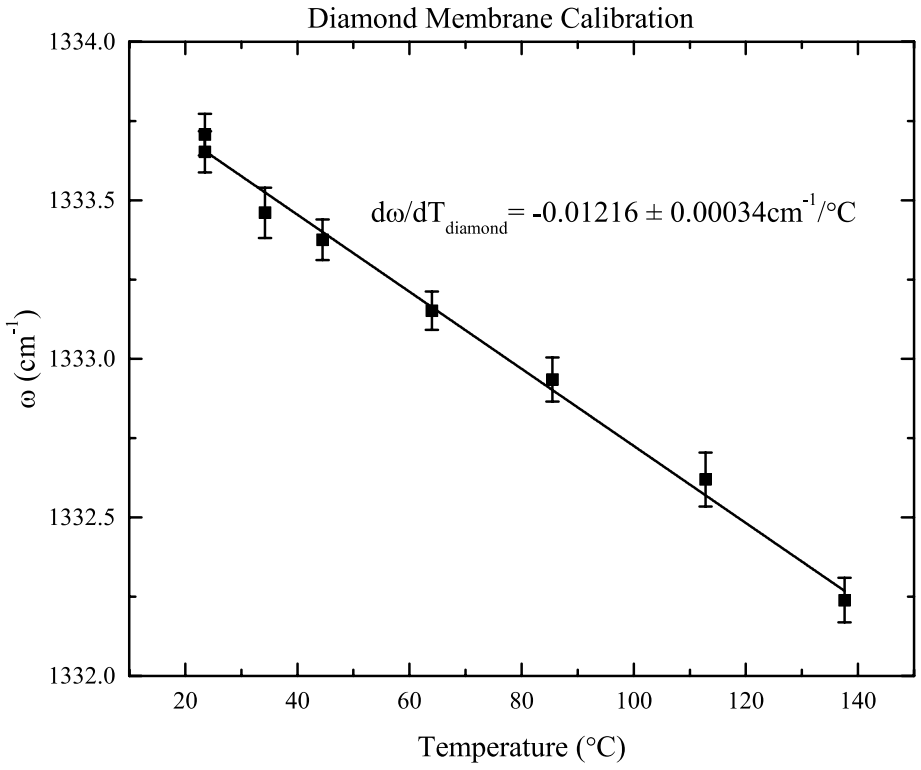

Figure 7: Diamond calibration. Raman temperature coefficient calibration measurement for the NRL A5L3 membrane. The sample was placed on a Peltier heater stage and the Raman shift was measured at various temperatures.

The sample was placed on two orthogonal Newport peizioelectric linear translation stages each with a step resolution of approximately 70 nm. Electrical contact probes were connected to either end of the heater structure. A Keithley 2401 was used to drive current through the heater while simultaneously measuring the voltage drop across the heater in order to calculate dissipated power. The micro-heater power was tuned such that the difference in the Raman shift (and thus the temperature rise) at the edge of the membrane was zero when compared to the "off" state. This was done in order to eliminate the need for accounting for thermal boundary resistance between the diamond film and the silicon substrate, thus simplifying the calculation. The Raman shift of diamond and h-BN at the membrane edge was recorded at room temperature as the initial Raman shift, ω_0.

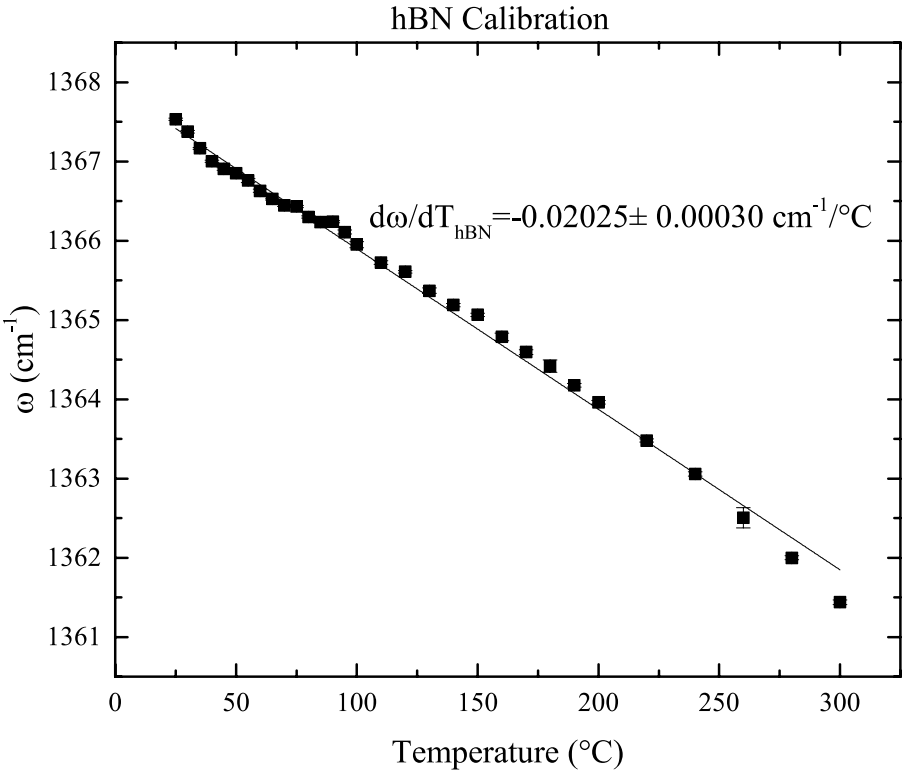

Figure 8: h-BN calibration. Calibration for determination of h-BN microparticle Raman temperature coefficient.

VI. EXPERIMENTAL RESULTS AND DISCUSSION

The membrane used for this study was 1mm in length and 202 μm wide. A 5 μm wide heater, centered at 95 μm from the edge, ran the length of the membrane. A second heater was located 168 μm from the same edge, and was not used in this study.

The sample was moved in increments of approximately 5 μm. The Raman spectrum was collected for 15 seconds at each point. Between steps, the CCD was triggered continuously at one-second intervals to search for h-BN particles. When h-BN was found, the stage was moved slowly in a single direction until the signal reached a maximum. Changes in direction were avoided in order to reduce spatial error due to backlash of the translation stage.

The spectra were fit with a Lorentzian curve-fitting algorithm in OriginPro™ 15. Batch processing was used to analyze all spectra simultaneously. The fitting parameters, such as peak position and linewidth, were constrained to limit misinterpreting cosmic ray peaks as real data. For spectra containing no h-BN signal, the "fit" h-BN data was removed, as a real signal was absent. The raw Raman shift data was converted to a temperature rise by dividing the difference in peak position by the calibration temperature coefficient.

$$\Delta T = \frac{(\omega_0 - \omega_i)}{\frac{d\omega}{dT}} \tag{59}$$

The data was corrected for spectrometer drift by subtracting a slope connecting the initial and final points (left to right). The results are presented below in Figure 8.

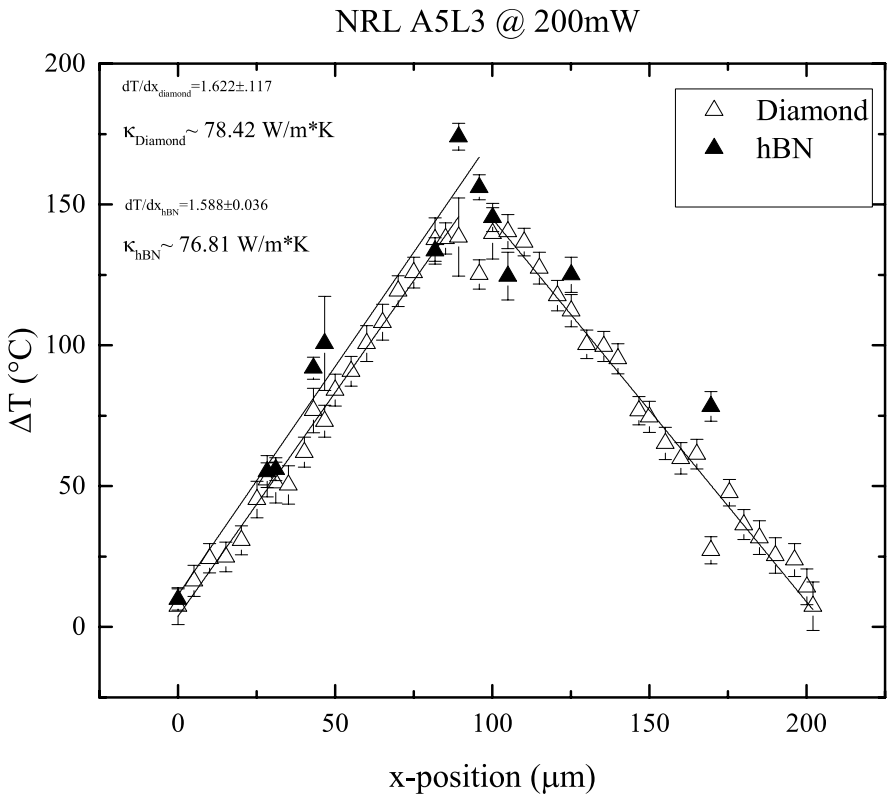

Figure 9: Temperature rise of diamond and h-BN. Results from a scan of device L3 of sample NRL A5. The slopes were fit linearly for diamond on either side of the heater. The slope for h-BN was fit linearly for the left side only. Thermal conductivities were calculated using the diamond and h-BN slopes, and are presented here.

An optical measurement of a material, especially at high laser power densities, will induce local heating of the sample at the precise location of the measurement. Therefore, it is necessary to verify that the laser power density used in this experiment is low enough that local heating is negligible. An optical power meter was placed on the sample stage. The power at the sample stage was measure as a function of laser current, which regulates output power, from approximately 10 μW to 1.2 mW at the sample. The Raman shifts of silicon, diamond, and h-BN were then

measured simultaneously as a function of laser current. The results are displayed in Figure 9.

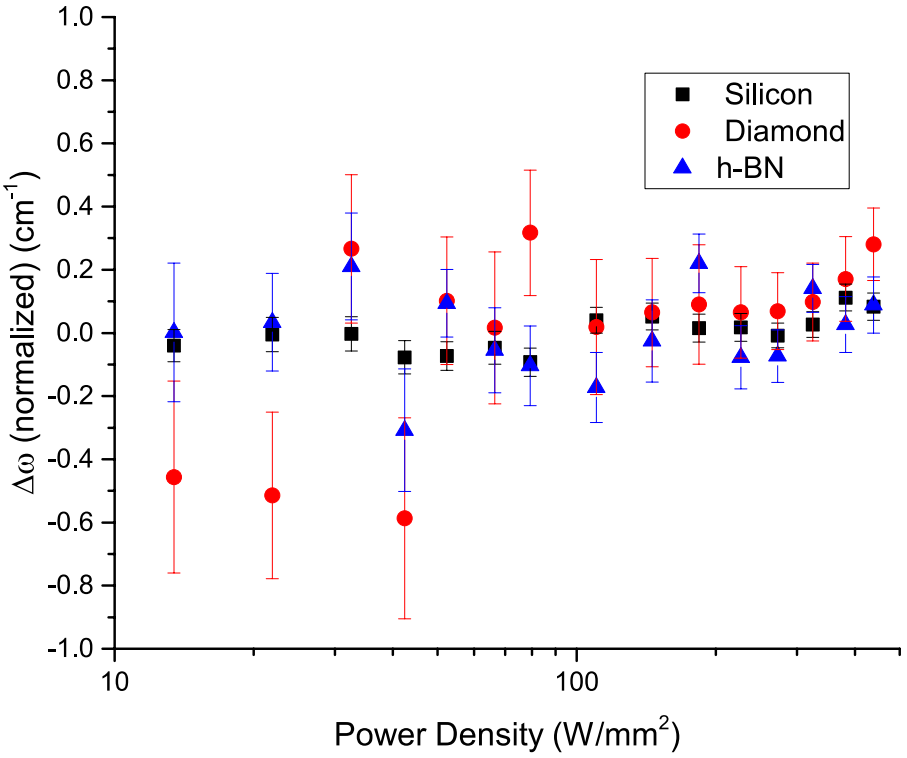

Figure 10: Power density considerations. The change in Raman shift is plotted against laser power density for silicon, diamond and h-BN. The data indicates that there is no significant local heating of the sample at high laser power.

The measured thermal conductivity of this diamond thin film is significantly smaller than for natural diamond ($\kappa_{natural} \approx 2200 \frac{\mathrm{W}}{\mathrm{m*K}}$). This is presumably due to a greatly reduced phonon mean free path (due to surfaces, grain boundaries, defects, dislocations, etc.). Surprisingly, the thermal conductivities calculated via diamond and h-BN particles are in good agreement. This indicates that the induced stress in this measurement is small enough to be neglected.

The h-BN data on top of the un-driven heater is elevated by ~10 °C compared with the diamond data. It is likely that the high laser power used in this experiment induced local heating of the metal. This can be eliminated by reducing the laser power to a low enough value.

The novel deposition method introduced here provides a stress free surface temperature measurement of *any* surface. Although metal surfaces experience slight local heating, the laser power may be lessened to perform the measurement. The simplicity and cost efficiency of the deposition process may be extremely appealing for industry. For example, a fully metalized, packaged, consumer-ready device may be temperature-mapped before distribution to ensure proper thermal management.

This work presents a novel micro/nano-particle deposition method to be used as surface Raman temperature probes. The method was successfully applied to a CVD diamond thin film membrane and h-BN temperature probes were used to corroborate Raman temperature data of diamond. The agreement of h-BN and diamond Raman temperature data suggests that the measurement was not perturbed by stress. Careful investigation of the effect of laser power density on laser heating suggests that the h-BN particles and diamond film experienced no significant local heating.

LITERATURE CITED

[1] J. Anaya, S. Rossi, M. Alomari, E. Kohn, L. Tóth, B. Pécz, and M. Kuball, Appl. Phys. Lett. **106**, 223101 (2015).

[2] A. Sood, J. Cho, K.D. Hobart, T.I. Feygelson, B.B. Pate, M. Asheghi, D.G. Cahill, and K.E. Goodson, J. Appl. Phys. **119**, 175103 (2016).

[3] T.M. Bandhauer, A. Agarwal, and S. Garimella, **41**, 1 (2005).

[4] K.E. Goodson, K. Kurabayashi, and R.F.W. Pease, IEEE Trans. Components Packag. Manuf. Technol. Part B **20**, 104 (1997).

[5] S. Weiß, E. Zakel, and H. Reichl, IEEE Trans. Components Packag. Manuf. Technol. Part A **19**, 46 (1996).

[6] I. Ahmad, V. Kasisomayajula, D.Y. Song, L. Tian, J.M. Berg, and M. Holtz, J. Appl. Phys. **100**, 1 (2006).

[7] T.J. Anderson and M.J. Tadjer, CS MANTECH Conf. 22 (2012).

[8] J. Cho, Y. Won, D. Francis, M. Asheghi, and K.E. Goodson, Tech. Dig. - IEEE Compd. Semicond. Integr. Circuit Symp. CSIC 1 (2014).

[9] M.J. Tadjer, T.J. Anderson, K.D. Hobart, T.I. Feygelson, J.D. Caldwell, C.R. Eddy, F.J. Kub, J.E. Butler, B. Pate, and J. Melngailis, IEEE Electron Device Lett. **33**, 23 (2012).

[10] O. Arenas, E. Al Alam, A. Thevenot, Y. Cordier, A. Jaouad, V. Aimez, H. Maher, R. Ares, and F. Boone, IEEE J. Electron Devices Soc. **2**, 145 (2014).

[11] S. Lani, C. Ataman, W. Noell, D. Briand, and N. de Rooij, Procedia Chem. **1**, 609 (2009).

[12] M. Zhao, X. Liu, Z. Yingkui, K. Wei, P. Mingzeng, L. Yankui, and L. Guoguo, 1 (n.d.).

[13] H. Kong, **8**, 1607 (1999).

[14] H. Peng, M.I.J. Stich, J. Yu, L.N. Sun, L.H. Fischer, and O.S. Wolfbeis, Adv. Mater. **22**, 716 (2010).

[15] G. Xu, S.K. Tripathy, X. Mu, Y.J. Ding, K. Wang, Y. Cao, D. Jena, and J.B. Khurgin, Appl. Phys. Lett. **93**, 2 (2008).

[16] M.S. Liu, L. a. Bursill, S. Prawer, K.W. Nugent, Y.Z. Tong, and G.Y. Zhang, Appl. Phys. Lett. **74**, 3125 (1999).

[17] R.B. Simon, J.W. Pomeroy, and M. Kuball, Appl. Phys. Lett. **104**, (2014).

[18] C. Kittel, *Introduction to Solid State Physics* (John Wiley & Sons, 2005).

[19] T.R. Anthony, W.F. Banholzer, J.F. Fleischer, L. Wei, P.K. Kuo, R.L. Thomas, and R.W. Pryor, Phys. Rev. B **42**, 1104 (1990).

[20] R.P. Mildren and J.R. Rabeau, *Intrinsic Optical Properties of Diamond* (2013).

[21] S. Prawer and R.J. Nemanich, Philos. Trans. A. Math. Phys. Eng. Sci. **362**, 2537 (2004).

[22] G. Davies, in *CVD Diam. Electron. Devices Sensors*, edited by R.S. Sussmann (Wiley, 2009).

[23] CassaboisG., ValvinP., and GilB., Nat Phot. **10**, 262 (2016).

[24] T.T. Tran, K. Bray, M.J. Ford, M. Toth, and I. Aharonovich, arXiv **11**, 1 (2015).

[25] Sampriti Bagchi, (2011).

[26] B.A. Weinstein and R. Zallen, in *Light Scatt. Solids IV*, edited by M. Cardona and G. Guntherodt (Springer-Verlag, 1984), pp. 463–525.

[27] H. Search, C. Journals, A. Contact, M. Iopscience, and I.P. Address, Europhys. Lett. **32**, 729 (1995).

[28] D.A. Long, *The Raman Effect: A Unified Treatment of the Theory of Raman Scattering by Molecules. 2002* (2002).

[29] M.-F. Li, *Modern Semiconductor Quantum Physics* (World Scientific, 1994).

[30] W. Hayes and R. Loudon, *Scattering of Light by Crystals* (John Wiley & Sons, 1978).

[31] A. Pinczuk and E. Burstein, in *Light Scatt. Solids*, edited by M. Cardona (Springer-Verlag, 1975), pp. 25–75.